Biointerface Research in Applied Chemistry
Open-Access Journal (ISSN: 2069-5837)

Article
Volume 14, Issue 3, 2024, 71
https://doi.org/10.33263/BRIAC143.071

Tribo-Mechanical Properties and Corrosion Study of Nano Zirconia Reinforced Electroless Ni-B Coatings

Deviprasanna Mohanty [1], Tapan Kumar Barman [1], Prasanta Sahoo [1,*]

[1] Department of Mechanical Engineering, Jadavpur University, Kolkata 700032, India
* Correspondence: psjume@gmail.com; prasanta.sahoo@jadavpuruniversity.in (PS)

Scopus Author ID 55562055400

Received: 21.03.2023; Accepted: 28.05.2023; Published: 17.02.2024

Abstract: The present investigation deals with studying zirconia-reinforced electroless Ni-B coatings deposited on mild steel substrates. The addition of ZrO_2 nanoparticles is assisted by ultrasonication, which helps form a uniform colloidal solution, which is then added to the coating bath. The coatings are deposited in varying zirconia concentrations (1 g/l, 5g/l, 10 g/l, and 15 g/l). The deposited coatings are investigated for Vicker's microhardness, elastic modulus, friction, wear, scratch width, and corrosion resistance. The results of the deposited coatings are also compared with binary Ni-B coatings. The coating with a zirconia concentration of 10 g/l in the bath shows the most promising result. This coating shows a decreased specific wear rate of nearly 1/3rd compared to the binary Ni-B coating. The coating with a zirconia concentration of 10g/l also shows improved corrosion resistance. The Ecorr of the coating shows an increase of approximately 13% towards a nobler value compared to the unreinforced coating (binary Ni-B coating). The same coating also shows an increase in the elastic modulus to nearly 14 % as compared to the binary Ni-B coating. The scratch width of the coating with 10 g/l zirconia concentration is minimum among the coatings under study. It is also observed that the above-mentioned properties deteriorated upon increasing the concentration of the nano-zirconia in the bath beyond 10 g/l.

Keywords: Electroless; Ni-B; Zirconia nanoparticles; Microstructure; Tribology; Corrosion.

1. Introduction

The use of coatings dates back to early civilizations that made coatings from natural materials such as plant extracts, animal hides, and mud to mostly protect their homes, weapons and hinting tools. However, the use of industrial coatings started in the early 19th century. The usage of coatings further broadened over the mid-1900s to cater to the needs of a variety of industries, including aerospace, marine, and electronics. The need of the hour was to develop coatings that could resist high temperatures, have anti-fouling characteristics, and provide electrical insulation. Hence, a number of coating methods came into existence. Each of these coating methods has a number of positives and negatives. Some examples of coating methods include thin film coatings, induction hardening, flame hardening, nitriding, carburizing, electrodeposition, and electroless deposition. The electroless coating process has many benefits and can coat any substrate, like ceramics, nonmetals, and metals. The process is also very straightforward and inexpensive. Electroless plating is an autocatalytic deposition method known for its versatility. These coatings are known to improve the properties of components used for machinery and equipment [1–7]. In this method of plating, a uniform coating of metal atoms is deposited onto the surface of the coating substrate due to a reaction between a reducer and a metallic salt that takes place in a solution bath within a defined temperature range. In the case of electroless plating, uniform coating can be generated even on complex shapes and non-

metallic surfaces [8]. In contrast, by an electroplating process, deposition is not possible on non-conducting surfaces. Electromagnetic shielding, functional coatings for oil and gas, decorative platings, and chemical, automotive, and aerospace industries are all dependent on the electroless coating process. Also, food, petrochemical, computer, plastics, and printing industries are some of the industries that use the electroless plating process [9–13]. A more recent application is reported by Yu *et al.* [14], about the improved stability of the Ni-cathode used in Ni ion batteries plated with electroless Ni-P. Yu *et al.* [15] have estimated the annual net growth rate of electroless Ni plating at 10% to 15%. Hence, it may be said that there is a need to further research and improve electroless coatings, which can enhance their ability to perform better with respect to their mechanical properties. Several researchers have worked towards improving the mechanical properties of the binary electroless Ni-B coatings by deploying different methods. The influence of various bath parameters on the coating properties has been reported by Barman *et al.* [16]. Tima and Mahboubi [17] have reported how the microstructure changes with plasma nitriding along with the effect it has on the wear behavior of the electroless Ni-B deposits. Recent research also aims to improve the environmental effect of such coatings [18-20].

One such way to improve the mechanical properties is by incorporating second-phase particles. The reinforcement of second-phase particles with a binary electroless Ni-B or Ni-P coating paves the way for an abundance of new opportunities [21]. The incorporation of these second-phase particles increases tensile strength, enhances resistance to corrosion and wear, and increase resistance to abrasion [1–7,22,23]. Although, it is possible to achieve a high level of hardness and wear resistance through heat treatment [24–26]. However, as the temperature rises, the corrosion resistance of the coatings will decrease [27]. Hence, the addition of nanoparticles is beneficial as it can improve both the mechanical properties and corrosion resistance of the coatings. Secondary particle reinforcement comes in two distinct varieties. The first category contains particles that are utilized to enhance the base material's properties, such as its resistance to wear, abrasion, and corrosion. These are primarily hard metal oxides, carbides, and nitrides [28–31]. Naturally, lubricious and soft particles fall into the second category [32–34]. Examples of this type of particle include polytetrafluoroethylene (PTFE), boron nitride, and molybdenum sulfide, among others. Although several articles have explored the characterization of mechanical properties [35-36], the evaluation of nanoparticle-reinforced coatings' tribo behavior is limited.

In the context of the current investigation, it is hypothesized that the incorporation of nano-zirconia will produce a coating that is more resistant to wear and corrosion, in addition to elevating the material's overall hardness. Due to the fact that zirconia has a bulk average hardness of approximately 10 GPa, the resulting composite coatings may have a higher bulk average hardness. Additionally, due to the size of these zirconia nanoparticles, it is anticipated that they will be able to cover the nodular gaps and pores of the softer Nickel-Boron matrix, which will result in the higher-quality coatings. The present research uses ultrasonication to form a colloidal solution of nanoparticles and water, which, when poured into the coating bath (continuously being stirred over a magnetic stirrer), helps deposit a coating with a uniform distribution of nanoparticles. The coatings have been examined using scanning electron microscopy, energy-dispersive X-ray spectroscopy, and X-ray powder diffraction in order to validate the aforementioned qualities.

2. Experimental Methods

2.1. Bath composition and sample preparation.

The mild steel samples undergo various cleaning methods before being deposited. This includes polishing the samples with emery papers using grades 800, 1200, 1600, and 2000 to render all the samples smooth and samples have the same surface roughness. This is followed by ultrasonic cleaning, acid pickling, and drying of the samples. The samples are then deposited in a chemical bath after being exposed to a heated $PdCl_2$ solution to make the surface more reactive for ease of deposition.

Table 1. Coating nomenclature.

Sl. No.	Coating description	Nomenclature
1.	Ni-B binary coating	Ni-B
2.	1 g/l ZrO_2 (nano) reinforced electroless Ni-B	Ni-B- 1g/l ZrO_2
3.	5 g/l ZrO_2 (nano) reinforced electroless Ni-B	Ni-B- 5g/l ZrO_2
4.	10 g/l ZrO_2 (nano) reinforced electroless Ni-B	Ni-B- 10g/l ZrO_2
5.	15 g/l ZrO_2 (nano) reinforced electroless Ni-B	Ni-B- 15g/l ZrO_2

Electroless Ni-B coatings are deposited over mild steel substrates. Also, coatings are deposited incorporating zirconia in the coatings. The coating nomenclature is given in Table 1. The bath composition is shown in Table 2. The bath solution is prepared in a volume of 250 ml in a clean beaker. The deposition is done using a magnetic stirrer (IKA, India) with a temperature control module. Nickel chloride hexahydrate acted as the source of Ni^{++} ions in the solution. Ethylenediamine is used as a complexing agent. The primary function of the complexing agents is to act as a deterrent and prevent the basic pH (12-14) of the solution from dropping steeply. Simultaneously, these complexing agents also help to prevent metallic nickel precipitation in the solution. Sodium borohydride provides the free electrons to reduce the Ni^{++} ions. A temperature of 85° ± 3° C was maintained throughout the deposition time of 1 hour. Before being introduced into the coating bath, the nano ZrO_2 was sonicated at 60 Hz in an ultrasonicator in deionized water.

Table 2. Bath composition.

Sl.No.	Chemical	Function	Amount in bath
1.	Nickel chloride	Nickel source	18-20gm/l
2.	Ethylene diamine	Complexing agent	45-50 ml/l
3.	Lead nitrate	Stabilizer	0.05-0.06 gm/l
4.	Sodium hydroxide	pH buffer	35-40 gm/l
5.	Sodium borohydride	Reducing agent	0.5 gm/l
6.	Nano Zirconia	Reinforcement	1 g/l, 5g/l, 10 g/l, 15 g/l
7.	SDS	Surfactant	2.36 gm

2.2. Surface morphology and elemental mapping.

In the present study, the coated specimens were characterized under the FESEM (Zeiss-SIGMA, Germany) to analyze the morphology. With SEM micrograph, visual evidence of nanoparticles was obtained. EDAX scan was performed to confirm the presence of various elements present. The SEM imaging was performed at 20 kV high tension voltages.

2.3. Hardness.

The Vicker's microhardness tester (UHL VMHT, Germany) was utilized to conduct measurements of microhardness. Micro Vickers hardness tester uses a diamond indenter to make indentations in the material being tested and then measures the diagonal length of the

indentation using a microscope. The hardness is calculated based on the applied load and the diagonal length of the indentation. The parameters used were an applied load of 100 gf, a dwell time of 15 seconds, and an indenter travel speed of 25 μm/s.

2.4. Elastic modulus.

Anton Parr NHT3 (Germany) nano-indentation tester is employed to obtain the elastic modulus of the coated samples. The method used involves allowing the load to vary until it reaches a maximum depth of 500 nanometers, after which the load is released. This technique is known as depth-sensing indentation and is commonly used to measure the mechanical properties of materials. The loading and unloading rates were carefully controlled and maintained at a rate of 20 mN/min to ensure accurate and reliable results.

2.5. Scratch test.

The scratch hardness was obtained using a Scratch tester (Ducom TR-101-IAS, India). The testing was done at a constant loading condition of 20N, 30N, and 40N. A Rockwell C-Type diamond indenter is used for scratching the samples. The diamond indenter has a flank angle of 120° and a radius of 200 μm. The specimen was scratched for a stroke length of 5mm and an indentation speed of 0.1mm/s. Scarview imaging software was used to obtain optical images.

2.6. Tribo test.

Tribo testing was performed using a wear and friction monitor (Ducom TR-208-M2, India). The tribotester employed is a pin-on-disc model, with the coated cylinders serving as the "pin" and the hardened EN31 disc serving as the counterface. The counter disc was rotated at a constant speed of 100 rpm, and the sliding distance was maintained at 500 m during the test. 1 kgf normal load was applied using the string and lever system. Average weight loss during the test was reported, and each was conducted three times. Acetone was used to remove any dirt or dust that accumulated on the counter disc due to use.

2.7. Corrosion test.

To investigate the electrochemical corrosion response of the coatings, a Potentiostat (ACM Instruments Gill AC, UK) was utilized. To collect the corrosion data, the three electrode potentiodynamic polarization method was used. A working electrode, a calomel electrode (saturated) for reference purposes, and a platinum electrode as a counter electrode are necessary requirements for this method. The sample under investigation is used as the working electrode, which had an exposed area of 1 cm^2. The corrosion tests are performed in a standard 3.5-weight percent sodium chloride (NaCl) solution [37]. Potentiodynamic scanning is conducted at a rate of 1 mV/s to obtain the corrosion data. Corrosion current densities and corrosion potential are determined through the Tafel extrapolation technique. This comprehensive method is used to ensure accurate and reliable data are obtained, aiding in the interpretation of the coating's corrosion behavior.

3. Results and Discussion

3.1. Microstructure.

Figure 1 shows the SEM microstructure of the coated specimen. The typical cauliflower-like microstructure is observed for the entire set of the specimen. During electroless deposition, the nucleation and growth of individual grains are responsible for this cauliflower-like morphology. The activated surface of the substrate provides excellent spots for the beginning of nucleation. The metallic ions of Ni-B then tend to overlap with each other and grow in a vertical direction, facilitating a columnar microstructure. Simultaneously, the Ni-B covers the nanoparticles and entraps the nanoparticles inside the porosities of these columnar growths.

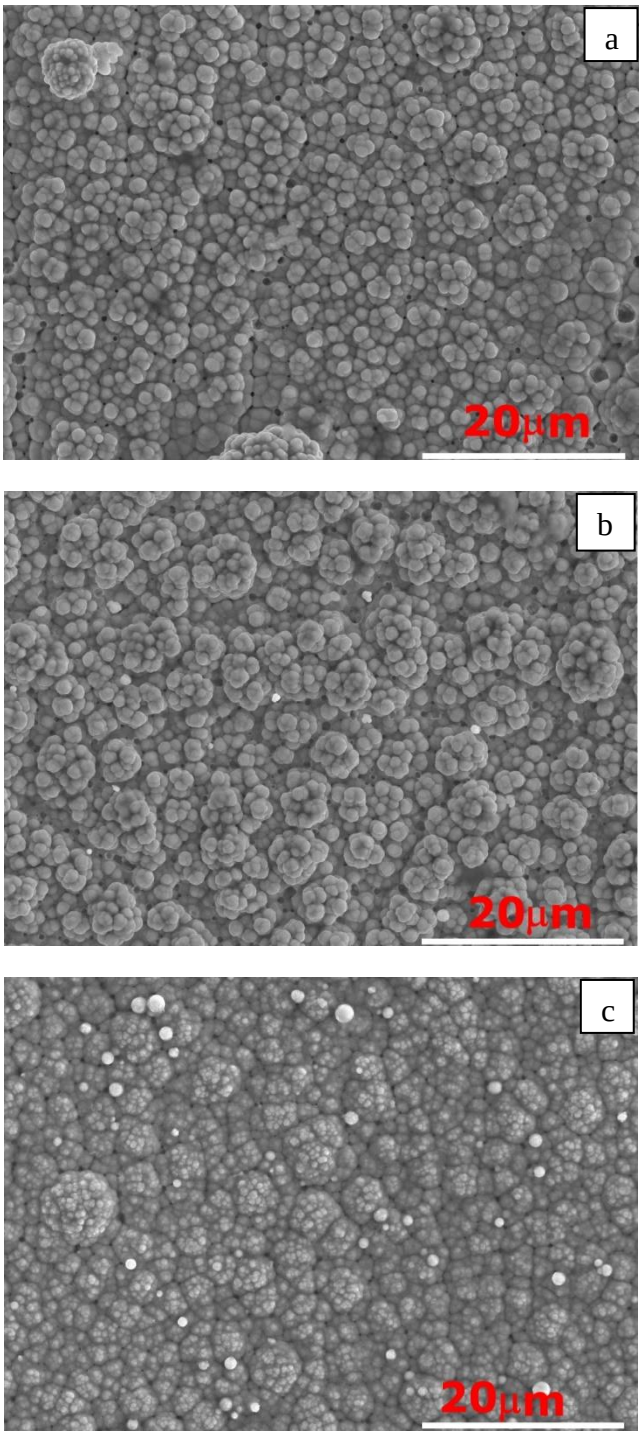

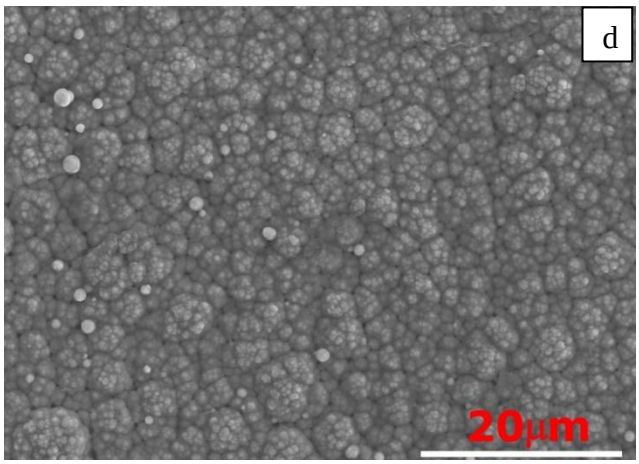

Figure 1. SEM image of **(a)** as deposited Ni-B, **(b)** as deposited Ni-B- 5g/l ZrO_2, **(c)** as deposited Ni-B- 10g/l, and **(d)** as deposited Ni-B- 15g/l ZrO_2 ZrO_2.

Figure 1 (b) to (d) shows the zirconia nanoparticles embedded in many such pores created due to the basic columnar microstructure of the electroless Ni-B matrix. Figure 1 (a) shows binary Ni-B coatings with porosities. Figure 1 (d) shows a lower presence of zirconia nanoparticles on the surface as compared to Figure 1 (c), although the amount of nanoparticles added to the coating is more for the coating shown in Figure 1 (c). This may be attributed to the fact that at a concentration of more than 10 g/l of zirconia nanoparticles, the agglomeration was higher. As a result, the adsorption of the nanoparticles was low. Also, as evident during the coating process, most of the nanoparticles settled at the bottom of the beaker and did not participate actively in the coating process.

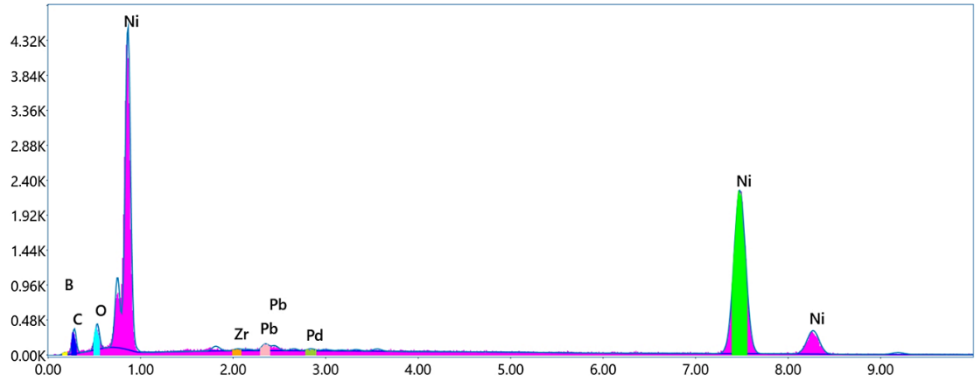

Figure 2. EDAX spectrum peaks of Ni-B-10 g/l ZrO_2.

The EDAX (Energy-dispersive X-ray analysis) spectra in Figure 2 show the presence of Boron, Oxygen, Zirconia, Lead, Palladium, and Nickel at their respective energy spectra. Palladium has been used as a surface activator, as evidenced by the presence in the EDAX scan. The EDAX scan shown in Figure 3 shows a uniform distribution of nano zirconia as observed from the distribution pattern of elemental Zr. The uniform distribution of nano zirconia is a result of ultrasonication. Ultrasonication facilitated the formation of a colloidal solution, which allowed the zirconia particles to remain in the solution throughout the coating without sedimenting. One of the primary requirements of a sound coating with reinforced nanoparticles is the homogenous distribution of the nanoparticles. As evident from the SEM images, the same has been achieved in the present study.

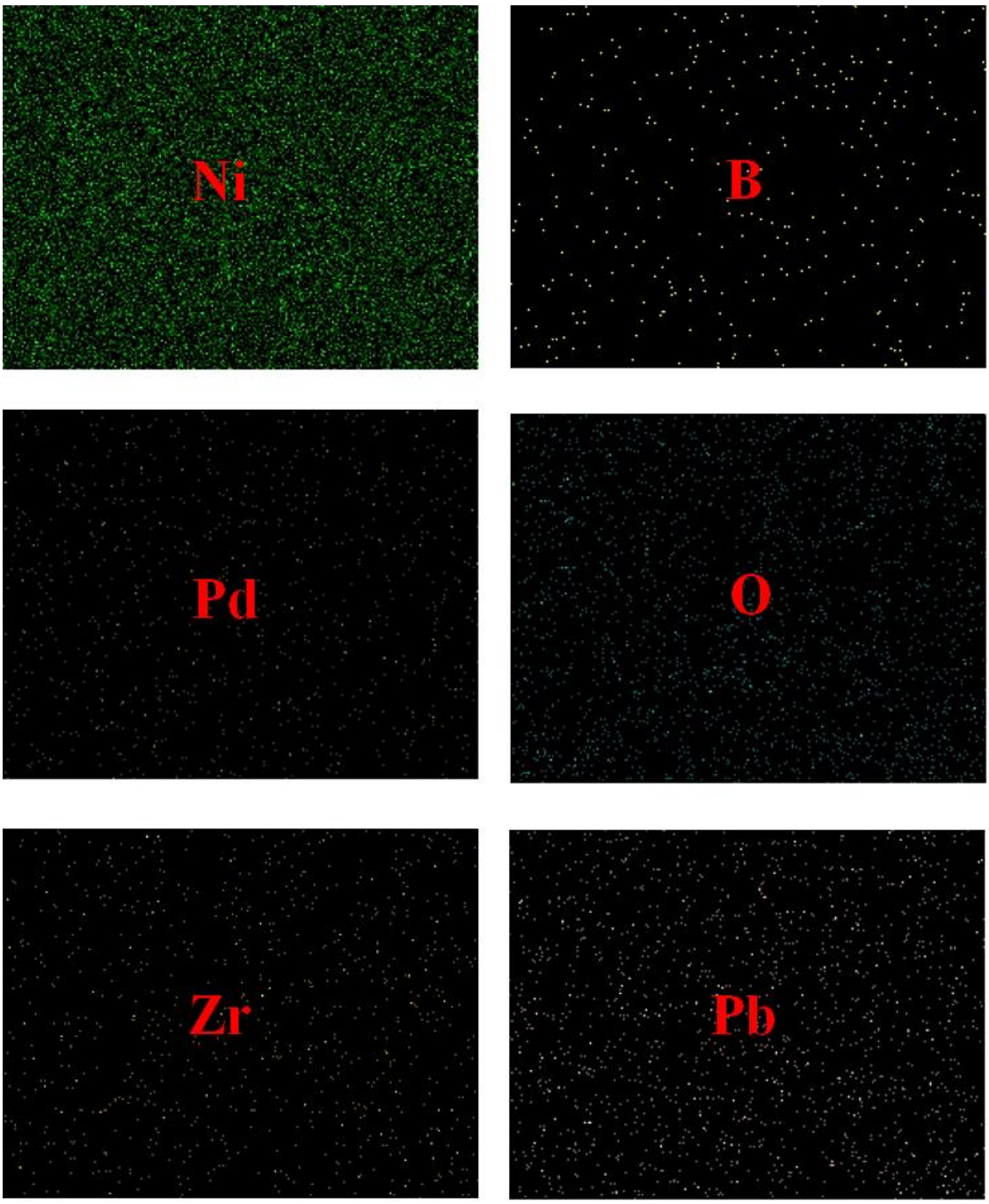

Figure 3. EDAX area scan of the surface of Ni-B-10 g/l ZrO_2.

3.2. Microhardness and elastic modulus.

Figure 4 shows the microhardness of the specimen under study. The expected increase in hardness occurs after the addition of nano-sized ZrO_2 particles. This can be attributed to the inclusion of the hard nanoparticles, which, when embedded in the more pliable Ni-B matrix, help share the load normally applied during the indentation hardness test. In addition, these nanoparticles impede the flow of material when a vertical load is applied during the test. This helps to restrict the size of the indentation, which ultimately leads to a higher value for the material's hardness. Even though the addition of nanoparticles results in an increase in the coating's hardness, at high concentrations of nanoparticles, the property deteriorates. This variation in hardness values is due to the inhomogeneous distribution of nano-ZrO_2 powders in the Ni-B-15 g/l ZrO_2 coatings, which is caused by a higher degree of agglomeration of alumina

beyond a concentration of 10 g/l. This agglomeration of alumina is what causes this deviation from the trend in hardness values. The elastic modulus of the as-deposited coatings is shown in Figure 5. The incorporation of nanoparticles results in an increase in the material's elastic modulus, which is more or less gradual. The elastic modulus (E) of the reinforced Ni-B-10g/l ZrO_2 coating is higher than that of the binary Ni-B coating, coming in at 83 GPa as opposed to 75.9 GPa. On further addition of nanoparticles, there is a drastic decrease in the modulus value to 75 GPa. This may be due to the higher degree of agglomeration, which tends to decrease the adsorption of the nanoparticles in the coating; as a result, their effectiveness in improving the overall elastic modulus decreases.

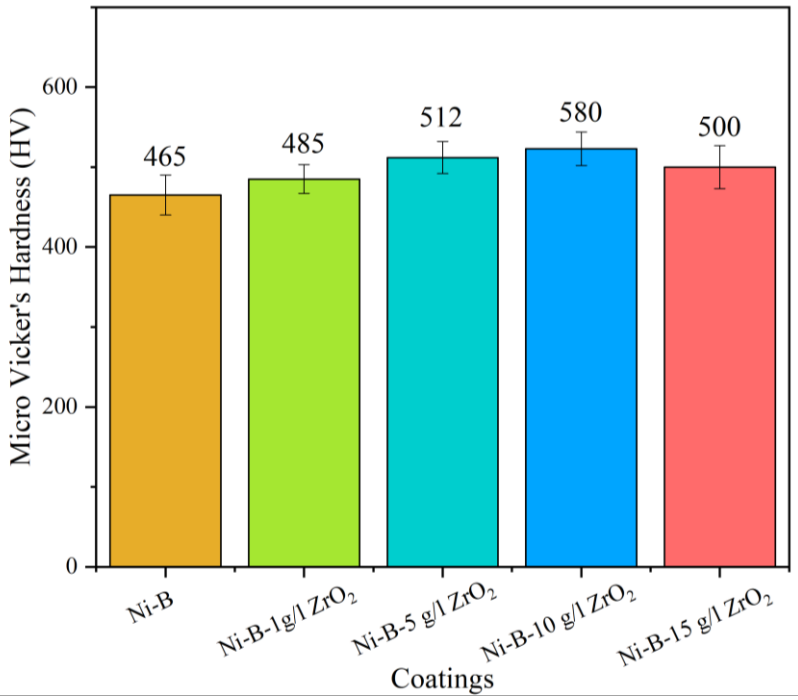

Figure 4. Vicker's microhardness.

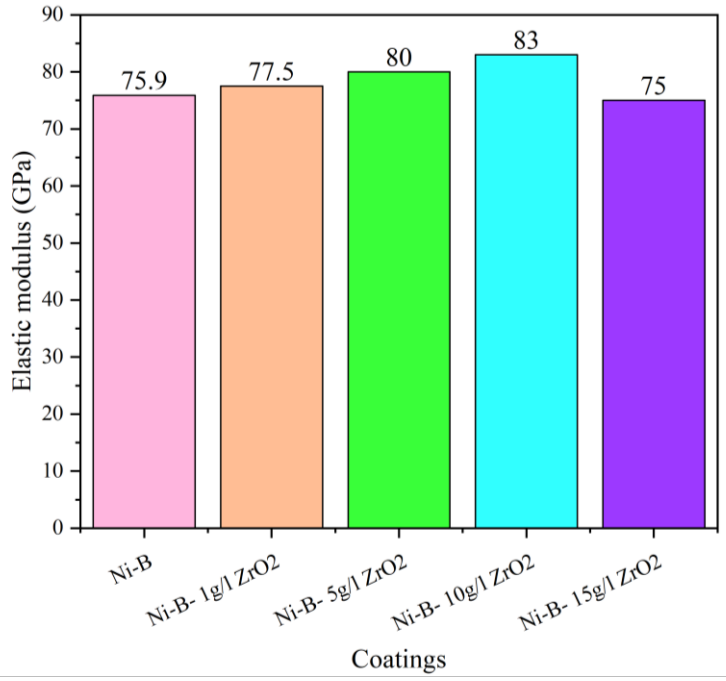

Figure 5. Elastic modulus of the coatings under study.

3.3. Wear behavior and wear mechanism.

Figure 6 shows the wear rate of specimens under study. Figure 7 shows the coefficient of friction values for the It is observed that with the addition of ZrO_2 nanoparticles, the specific wear rate of the samples increased initially up to a nanopowder concentration of 10 g/l but with a further increase, the wear resistance decreased. As a result, the wear rate increased.

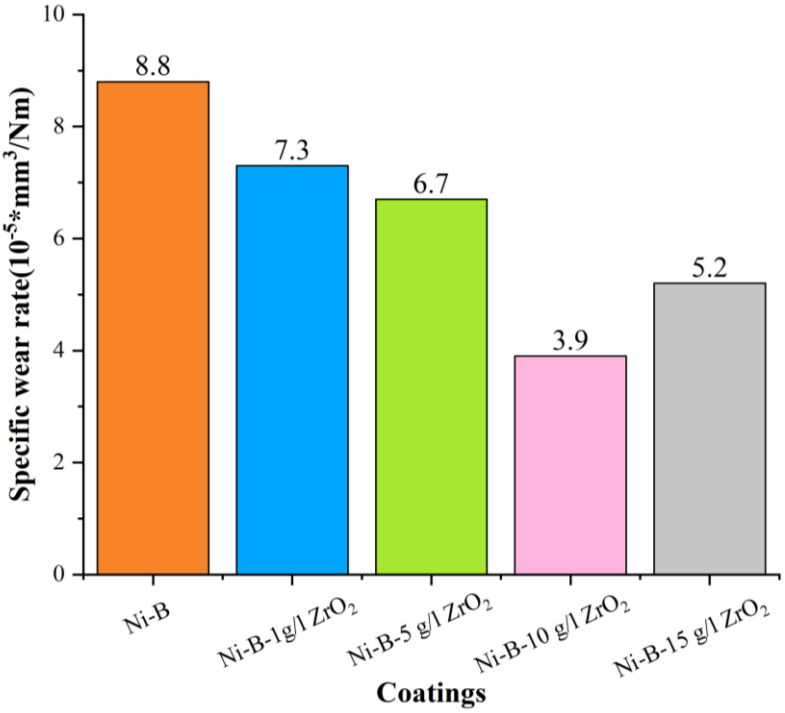

Figure 6. The specific wear rate of the as-deposited binary Ni-B coating and reinforced coatings.

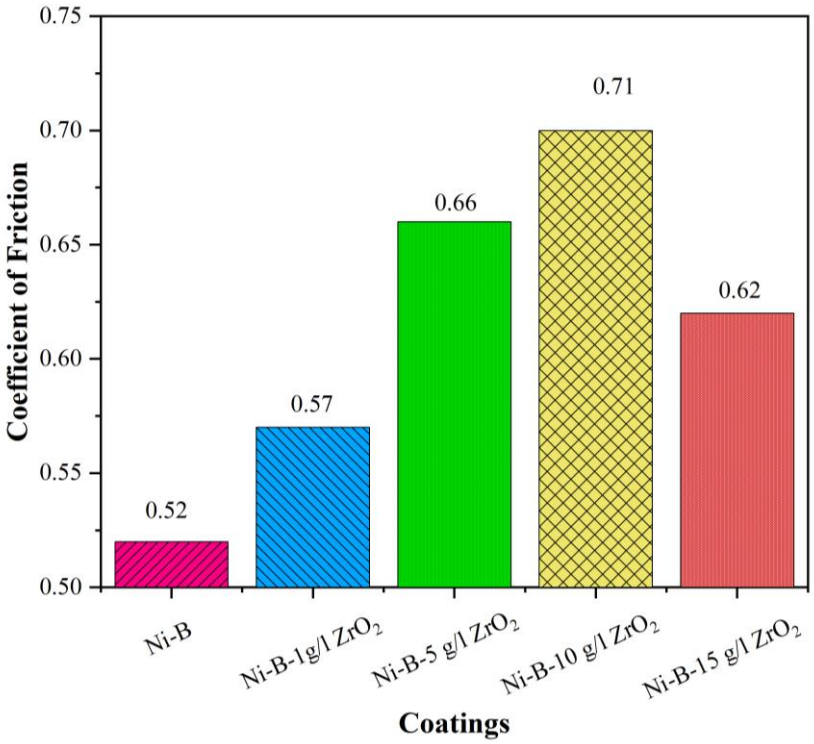

Figure 7. The specific wear rate of the as-deposited binary Ni-B coating and reinforced coatings.

The specific wear rate for Ni-B, Ni-B- 1 g/l ZrO_2, Ni-B- 5 g/l ZrO_2, Ni-B- 10 g/l ZrO_2 and Ni-B- 15 g/l ZrO_2 are 8.8 x 10^{-5} mm^3/Nm, 7.3 x 10^{-5} mm^3/Nm, 6.7 x 10^{-5} mm^3/Nm, 3.9 x

10^{-5} mm^3/Nm and 5.2 x 10^{-5} mm^3/Nm, respectively. This is due to the fact that the nanoparticles perform multiple functions which affect the wear resistance of the coating. Firstly, these embedded nanoparticles obstruct the dislocation motion and do not easily allow the dislocation to flow through the coating. This slows down the process of deformation and, finally, material failure. Secondly, these particles increase the frictional force; hence, more load is required to remove the material (coating). Finally, they act as load-bearing members and help distribute the applied material throughout the coating; thus, they do not allow the stress to concentrate at a place that may be detrimental to the wear resistance behavior of the coating. This may be attributed to higher nanoparticle concentrations, which inherently exhibit high surface energy and contribute to a high agglomeration rate. This causes the nanoparticles to accumulate in large volumes and sediment to the bottom of the beaker during the coating. The adsorption of the nanoparticles into the coating decreases and makes the addition of nanoparticles less effective compared to coatings with lower concentrations of nanoparticles. As the addition of nanoparticles increases, the friction coefficient increases, as shown in Figure 7. Overall, it may be said that with the addition of nanoparticles up to a certain concentration (10 g/l), the wear resistance and friction coefficient increase.

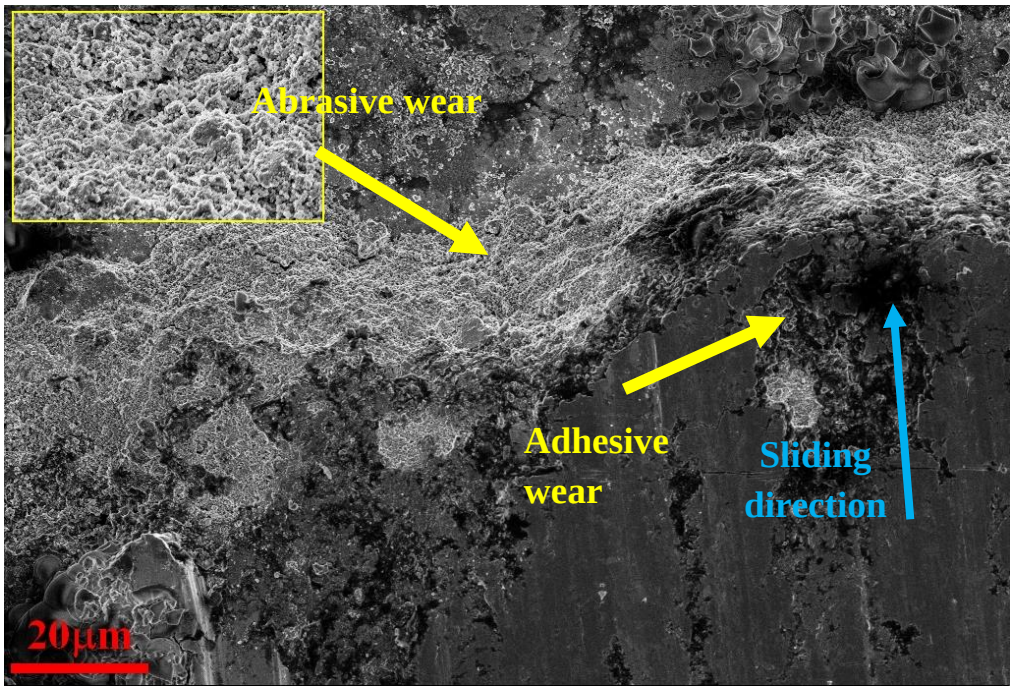

Figure 8. SEM image showing the wear morphology of Ni-B-10 g/l ZrO_2.

Figure 8 shows the SEM image of the worn surface of Ni-B-10 g/l ZrO_2 coating. The wear morphology shows both adhesive and abrasive wear. The worn surface shows coating pluck out, which is typical of adhesive wear, where, due to localized welding, the top surface of the specimen attaches to the counter face. This welded protrusion, at a later stage, breaks due to the continuous sliding motion between the specimen and the counterface. This creates a crater, as seen in Figure 8, indicating adhesive wear. On the other hand, there is also evidence of abrasive wear due to three body abrasions brought about by the presence of agglomerated nanoparticles between the sliding surfaces. This results in smaller debris stuck onto the worn surface, as seen in Figure 8. Hence, it may be observed that the wear phenomenon is a combination of both abrasive and adhesive wear.

3.4. Scratch resistance.

Figures 9 (a) and (b) show the scratches on the Ni-B and Ni-B-ZrO_2 coatings, respectively. Figure 9 (c) shows the scratch width values of the specimen. The scratch hardness for a set of applied loads (20 N, 30 N, and 40 N) increases with the addition of ZrO_2 in the coatings. The best results are obtained for higher Ni-B-10 g/l ZrO_2 coating. This can be attributed to the inclusion of hard ZrO_2 nanoparticles, which are found to be embedded in the as-deposited Nickel-Boron matrix. Also, at a very high concentration of 15 g/l, the hardness decreased as the amount of adsorption of ZrO_2 decreased due to a high degree of agglomeration. These hard particles obstruct penetration, resulting in a lower scratch width.

From Figure 9 (c), it is observed that the minimum scratch width is obtained for the Ni-B-10 g/l ZrO_2 for all the applied loads. The trend of decreasing scratch width is observed with the addition of ZrO_2 up to a concentration of 10 g/l; thereafter, the scratch width increases for all applied loads for the coating Ni-B-15 g/l ZrO_2. This is because, at higher concentrations, the nanoparticles agglomerate and do not contribute to improving the coating properties.

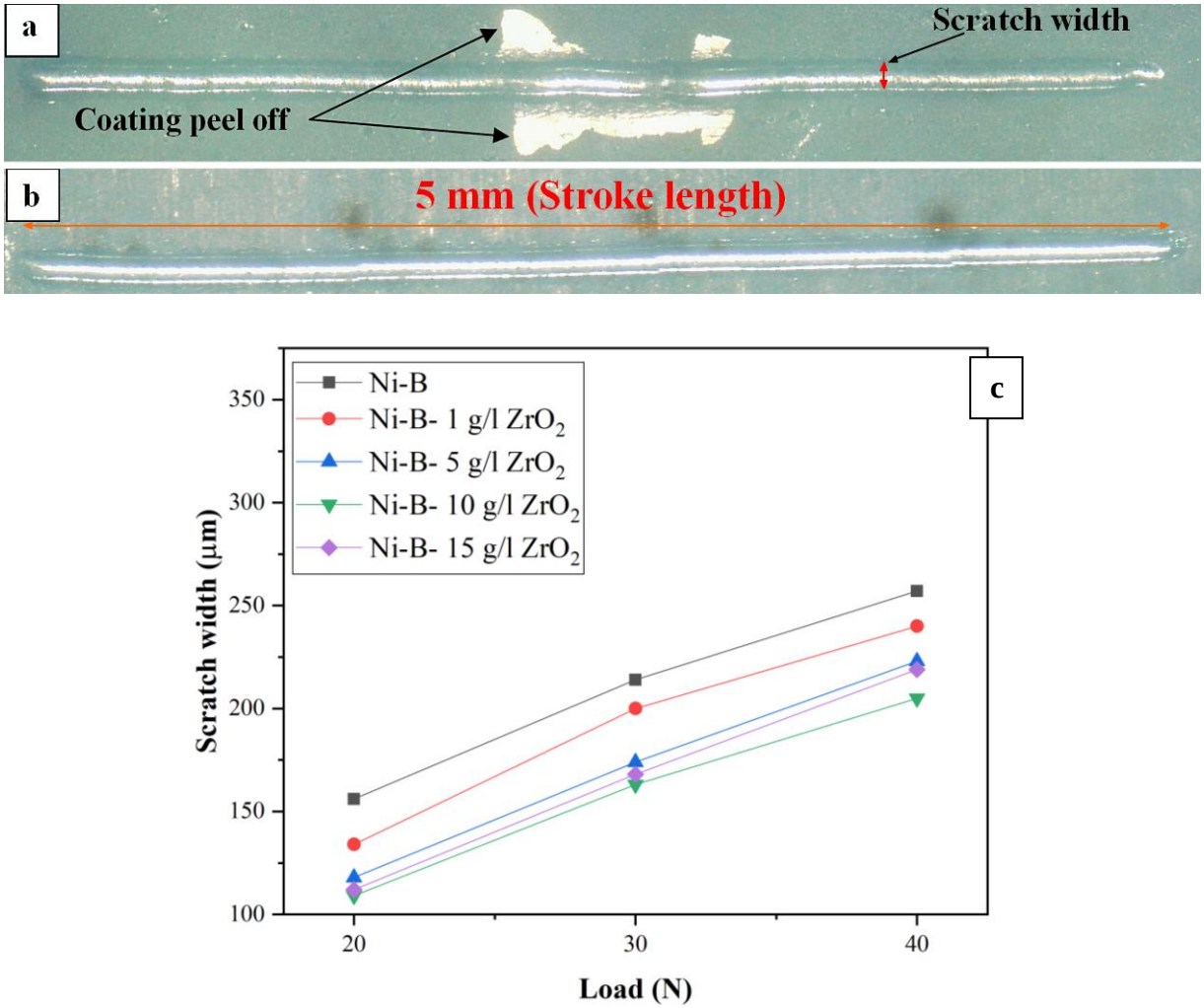

Figure 9. Optical image of **(a)** as deposited Ni-B, **(b)** Ni-B- 10 g/l ZrO_2, and **(c)** Scratch width obtained at varying loads of 20 N, 30 N, and 40 N.

3.5. Corrosion.

Figure 10 shows the Tafel curves, and Figure 11 shows the Nyquist plots for all the coatings under study. The slope of the anodic and cathodic parts is shown in Table 3. The

electrochemical corrosion test is done using the commonly used three-electrode method. In the case of Ni-B and Ni-B-5 g/l ZrO_2, the anodic corrosion is more dominant over the cathodic corrosion as indicated by a much higher value of β_a (anodic slope) compared to β_c (cathodic slope). The rest of the coatings show more balanced anodic and cathodic corrosion. The E_{corr} also shifts to a nobler value for the coatings with higher concentrations of nanoparticles. The best corrosion potential value is obtained for Ni-B-10 g/l ZrO_2 at -428.31 mV. Compared to the binary Ni-B coating with a value of -494 mV, the Ni-B-10 g/l ZrO_2 coating showed an improvement of around 13 %. However, it should be noted that the corrosion current density and not the corrosion potential are the determining factors in the corrosion resistance property of a material. In the present study, the corrosion current density I_{corr} for the Ni-B-10 g/l ZrO_2 is the least; hence, this coating has the highest corrosion resistance to the standard corrosion environment of 3.5 % NaCl. The R_{ct} value increases with the addition of nanoparticles.

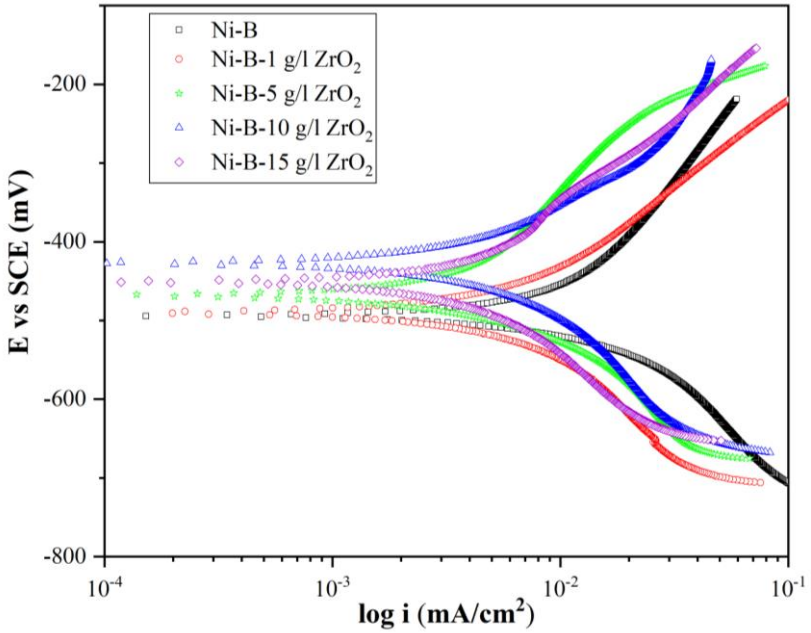

Figure 10. Tafel curves of the as-deposited coatings.

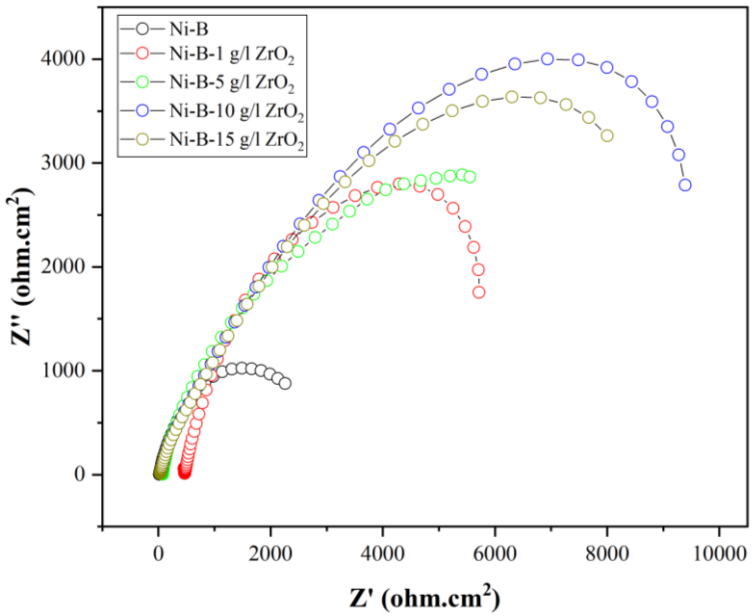

Figure 11. Nyquist plot for the coatings under study.

The R_{ct} value is calculated from a semicircle fit into the EIS plot shown in Figure 11. The values of Ecorr, Icorr, and Rct are shown in Table 3. The R_{ct} value of Ni-B-10 g/l ZrO_2 is 5 times that of the binary as deposited Ni-B. The coating Ni-B-15 g/l ZrO_2 does not follow the trend and shows an R_{ct} value of 1.1 x 10^4 which shows a lower corrosion resistance as compared to Ni-B-10 g/l ZrO_2. This may be due to the lower degree of adsorption of ZrO2 in the Ni-B-15 g/l ZrO_2 coating owing to high agglomeration.

Table 3. Corrosion data obtained from the Tafel plot and the Nyquist plot.

Coating	E_{corr} (mV)	I_{corr} (mA/cm^2)	β_a (mV/dec)	β_c (mV/dec)	R_{ct} (ohms.cm^2)
Ni-B	-494	0.011	365.8	196.5	0.3x10^4
Ni-B- 1 g/l ZrO_2	-491.6	0.004	152.2	151.7	0.8x10^4
Ni-B- 5 g/l ZrO_2	-468.1	0.0031	188.3	105	1.04x10^4
Ni-B- 10 g/l ZrO_2	-428.3	0.0028	98	95	1.5x10^4
Ni-B- 15 g/l ZrO_2	-451	0.003	209.6	207.6	1.1x10^4

4. Conclusions

Ni-B, Ni-B- 1g/l ZrO2, Ni-B- 5g/l ZrO2, Ni-B-10 g/l ZrO2 and Ni-B- 15 g/l ZrO_2 coatings were deposited with uniformly distributed ZrO_2 and good coating adhesion. The tests performed on these coatings revealed Ni-B- 10 g/l ZrO_2 to be the best among the as-deposited coatings. The conclusions from the findings are given below.

The Vickers microhardness value for Ni-B- 10 g/l ZrO_2 was found to be 580 HV as compared to the 465 HV for as-deposited binary Ni-B. With a further increase of ZrO2 concentration to 15 g/l the hardness decreased to 500 HV.

The elastic modulus gradually increased from 73 GPa for as-deposited Ni-B to 83 GPa for Ni-B- 10 g/l ZrO_2.

The specific wear rate of the Ni-B-10 g/l ZrO_2 decreased by nearly 1/3rd to 3.2 x 10-5 mm3/ Nm compared to 8.8 x 10-5 mm3/ Nm for Ni-B coating. An increase in the friction coefficient was also observed with the addition of zirconia nanoparticles up to a concentration of 10 g/l, but with further addition, the friction coefficient decreases, i.e., for the coating Ni-B-15 g/l ZrO_2.

The scratch width decreases with the addition of the zirconia nanoparticles. The decrease in width for the Ni-B-10 g/l ZrO_2 coating is found to be around 34 %, 28 %, and 23 % for the applied load of 20 N, 30 N, and 40 N, respectively, as compared to the binary Ni-B coating.

The corrosion resistance of Ni-B-10 g/l ZrO_2 is the best among the coatings under study. The Ecorr decreases from a value of – 494 mV for Ni-B to a nobler value of – 428 mV Ni-B-10 g/l ZrO_2. The Rct decreases from 0.3 x 104 ohms.cm2 for Ni-B to 1.5 x 104 ohms.cm^2 for Ni-B-10 g/l ZrO_2. The Icorr decreases to 0.0028 mA/cm2 for Ni-B-10 g/l ZrO_2 as compared to the unreinforced Ni-B coating, which has a high corrosion current density of 0.011 mA/cm^2.

Overall it is seen that the Ni-B-10 g/l ZrO_2 coating shows the most improved results in comparison to the other coatings.

Funding

This research received no external funding.

Conflicts of Interest

No conflict of interest is declared by the authors for the current work.

References

1. Gadhari, P.; Sahoo, P. Electroless Nickel-Phosphorus Composite Coatings : A Review. *Int. J. Manuf. Mater. Mech. Eng.* **2016**, *6*, 14-50, https://doi.org/10.4018/IJMMME.2016010102
2. Loto, C.A. Electroless Nickel Plating – A Review. *Silicon* **2016,** *8*, 177–186, https://doi.org/10.1007/s12633-015-9367-7
3. Sudagar, J.; Lian, J.; Sha, W. Electroless nickel , alloy , composite and nano coatings – A critical review. *J. Alloys Compd.* **2013**, *571*, 183–204, https://doi.org/10.1016/j.jallcom.2013.03.107
4. Sankara Narayanan, T.S.N.; Seshadri, S.K. Formation and characterization of borohydride reduced electroless nickel deposits. *J. Alloys Compd.* **2004,** *365*, 197–205, https://doi.org/10.1016/S0925-8388(03)00680-7
5. Delaunois, F.; Lienard, P. Heat treatments for electroless nickel – boron plating on aluminium alloys. *Surf. Coat. Technol.* **2002**, *160*, 239–248, https://doi.org/10.1016/S0257-8972(02)00415-2
6. Gilley, K.L.; Nino, J.C.; Riddle, Y.W.; Hahn, D.W.; Perry, S.S. Heat Treatments Modify the Tribological Properties of Nickel Boron Coatings. *ACS Appl. Mater. Interfaces*. **2012,** *8*, 3069–76, https://doi.org/10.1021/am3004297
7. Ghaderi, M.; Rezagholizadeh, M.; Vaghefi, S.M.M.; Heidary, A. Investigation of High Temperature Wear Resistance of Electroless Nickel Coating with Different Contents of Phosphorous. *Prot Met Phys Chem Surf.* **2016**, *52*, 538–542, https://doi.org/10.1134/S2070205116030126
8. Dang, X.; Cui, K.; Zhuang, J.; Zhong, L.; He, Y.; Li, G.; Du, G.; Yang, Z.; Pei, S.; Li, S. A new environmentally friendly non-destructive activation process of electroless nickel plating on alumina ceramics. *Mater. Today Commun*. **2023**, *35*, 105506, https://doi.org/10.1016/j.mtcomm.2023.105506
9. Çelik, I.; Karakan, M.; Bülbül, F. Investigation of structural and tribological properties of electroless Ni-B coated pure titanium. *Proc. Inst. Mech. Eng. Part J J. Eng. Tribol.* **2016,** *230*, 57–63, https://doi.org/10.1177/1350650115588568
10. Domínguez-Ríos, C.; Hurtado-Macias, A.; Torres-Sánchez, R.; Ramos, M.A.; González-Hernández, J. Measurement of mechanical properties of an electroless Ni-B coating using nano-indentation. *Ind. Eng. Chem. Res.***2012,** *51*, 7762–7768, https://doi.org/10.1021/ie201760g
11. Bülbül, F.; Altun, H.; Küçük, O.; Ezirmik, V. Tribological and corrosion behaviour of electroless Ni-B coating possessing a blackberry like structure. *Met. Mater. Int.***2012,** *18*, 631–637, https://doi.org/10.1007/s12540-012-4011-1
12. Das, S.K.; Sahoo, P. Tribological characteristics of electroless Ni-B coating and optimization of coating parameters using Taguchi based grey relational analysis. *Mater. Des.* **2011,** *32*, 2228–2238, https://doi.org/10.1016/j.matdes.2010.11.028
13. Sahoo, P.; Das, S.K. Tribology of electroless nickel coatings - A review, *Mater. Des.***2011,** *32*, 1760–1775, https://doi.org/10.1016/j.matdes.2010.11.013
14. Yu, D.; Yuan, Z.; Li, X. Enhanced stability of nickel cathode for nickel-based batteries by electroless nickel phosphide plating. *Chem. Eng. Sci.* **2023,** *270*, 118512, https://doi.org/10.1016/j.ces.2023.118512
15. Yu, X.; Hou, Y.; Ren, X.; Sun, C.; Wang, M. Research progress on the removal, recovery and direct high-value materialization of valuable metal elements in electroplating/ electroless plating waste solution. *J. Water Process Eng.* **2022**, *46*, 102577, https://doi.org/10.1016/j.jwpe.2022.102577
16. Barman, M., Barman, T.K.; Sahoo, P. Effect of coating bath parameters on properties of electroless Nickel-Boron alloy coatings. *Int. J. Surf. Eng. Interdiscip. Mater. Sci.* **2022**, *10*, 1–26, https://doi.org/10.4018/IJSEIMS.2022010101
17. Tima, R.; Mahboubi, F. Effect of plasma nitriding temperature on microstructure and wear properties of electroless nickel-boron coatings. *Surf. Coatings Technol.* **2021,** *415*, 127084, https://doi.org/10.1016/j.surfcoat.2021.127084
18. Cheng A. Y.; Sheu, H. H.; Huang P. C.; Liu, Y. M.; Pu, N.W.; Ger,M.D. Evaluation of alternative environment-friendly buffers for Ni–B alloy electroplating, *J. Mater. Res. Technol.* **2022**, *21*, 679–691, https://doi.org/10.1016/j.jmrt.2022.09.050
19. Agrawal, R.; Mukhopadhyay, A. Inclusion of W in electroless Ni–B coating developed from a stabilizer

free bath and investigation of its tribological behaviour, *J. Indian Chem. Soc.* **2023,** *100*, 100966, https://doi.org/10.1016/j.jics.2023.100966

20. M. Driouch, M.; EL Haloui, A.; EL Assiri, E.H.; Achnine, N.; Sfaira, M.; Touhami, M.E.; Kaya, S.; Zarrouk, A. Tyrosine as a novel potential stabilizer in an electroless Ni-P bath exempt of trisodium citrate as complexing agent: Chemical baths optimization and comparative study, *Chem. Data Collect.* **2022**, *37*, 100801 https://doi.org/10.1016/j.cdc.2021.100801
21. Vitry, V.; Hastir, J.; Mégret, A.; Yazdani, S.; Yunacti, M.; Bonin, L. Recent advances in electroless nickel-boron coatings. *Surf. Coatings Technol.* **2022**, *429*, 127937, https://doi.org/10.1016/j.surfcoat.2021.127937
22. J.N. Balaraju, J.N. T.S.N. Sankara Narayanan, S.K. Seshadri. Electroless Ni-P composite coatings. *J. Appl. Electrochem.* **2003**, *33*, 807–816 https://doi.org/10.1023/A:1025572410205
23. Krishnaveni, K.; Sankara Narayanan, T.S.N.; Seshadri, S.K. Electroless Ni-B-Si_3N_4 Composite Coating: Deposition and Evaluation of Its Characteristic Properties. *Synth. React. Inorganic, Met. Nano-Metal Chem.* **2012**, *42*, 920–927 https://doi.org/10.1080/15533174.2011.618475
24. Biswas, A.; Das, S.K.; Sahoo, P. Effect of copper incorporation on phase transformation behavior of electroless nickel–phosphorous coating and its effect on the tribological behavior. *Proc. Inst. Mech. Eng. Part L J. Mater. Des. Appl.* **2021**, *235*, 898–916, https://doi.org/10.1177/1464420720981602
25. Biswas, P.; Das, S.K.; Sahoo, P. Role of heat treatment on the friction and wear behavior of duplex electroless nickel deposits, *Mater. Today Proc.* **2022**, *66*, 3902–3909, https://doi.org/10.1016/j.matpr.2022.06.322
26. Barman, M.; Barman, T.K.; Sahoo. P. Tribo-mechanical characterization of ENB alloy coatings: effect of heat-treatment temperature and sodium borohydride concentration. *Facta Univ. Ser. Mech. Eng.* **2022**, https://doi.org/10.22190/FUME220814041B
27. Dervos, C.T.; Novakovic, J.; Vassiliou, P. Vacuum heat treatment of electroless Ni-B coatings. *Mater. Lett.* **2004**, *58*, 619–623, https://doi.org/10.1016/S0167-577X(03)00581-0.
28. Grosjean, A.; Rezrazi, M.; Takadoum, J.; Berc, P. Hardness, friction and wear characteristics of nickel-SiC electroless composite deposits. *Surf. Coat. Technol.* **2001,** *137*, 92–96, https://doi.org/10.1016/S0257-8972(00)01088-4
29. Alirezaei, S.; Monirvaghefi, S.M.; Salehi, M.; Saatchi, A. Effect of alumina content on surface morphology and hardness of Ni-P-Al_2O_3 (a) electroless composite coatings. *Surf. Coat. Technol.* **2004**, *184*, 170–175, https://doi.org/10.1016/j.surfcoat.2003.11.013
30. Aal, A.A.; Hassan, H.B.; Rahim, M.A.A. Nanostructured Ni-P-TiO_2 composite coatings for electrocatalytic oxidation of small organic molecules. *J. Electroanal. Chem.* **2008** *620*, 17–25, https://doi.org/10.1016/j.jelechem.2008.03.004
31. Bhattacharyya, S.; Mohanty, D.; Kumar, P., Das, S.K.; Sahoo, P.; Pal, S.K.; Chakraborty. S. A corrosion and tribo-failure analysis of Ni-P-Cu coated mild steel (AISI-1040) at varied copper concentration. *Eng. Fail. Anal*. **2023,** *146*, 107063, https://doi.org/10.1016/j.engfailanal.2023.107063
32. Leo, O.A., Staia, M.H.; Hintermann, H.E. Wear mechanism of Ni-P-BN (h) composite autocatalytic coatings. *Surf. Coat. Technol.* **2004,** *200*, 1825–1829, https://doi.org/10.1016/j.surfcoat.2005.08.061
33. Hu, X.G.; Cai, W.J. Xu, Y.F.; Wan, J.C.; Sun, X.J. Electroless (Ni-P-MoS_2) composite coatings and their corrosion properties. Surf. Eng. **2009**, *25*, 361–366, https://doi.org/10.1179/174329408X282532
34. Sharma, A.; Singh. A.K. Corrosion and wear resistance study of Ni-P and Ni-P-PTFE nanocomposite coatings. *Open Eng.* **2011,** *1*, 234-243, https://doi.org/10.2478/s13531-011-0023-8
35. Ekmekci, D.; Bülbül, F. Preparation and characterization of electroless Ni–B/nano-SiO_2, Al_2O_3, TiO_2 and CuO composite coatings. *Bull. Mater. Sci*. **2015**, *38*, 761-768, https://doi.org/10.1007/s12034-015-0912-1
36. Wang, S. J., Wang, Y., Shu, X., Tay, S., Gao, W., Shakoor, R. A., & Kahraman, R. Preparation and property of duplex Ni–B–TiO2/Ni nano-composite coatings. *Int. J. Mod. Phys. B.* **2015**, *29*, 1540022, https://doi.org/10.1142/S0217979215400226
37. Zhang, Y.; Shen, X. Facile fabrication of robust superhydrophobic coating for enhanced corrosion protection on AZ91 magnesium alloy by electroless Ni-B/GO plating, *Surf. Coatings Technol.* **2023**, *455*, 129213, https://doi.org/10.1016/j.surfcoat.2022.129213